NJC

ROYAL SOCIETY OF CHEMISTRY

PAPER

View Article Online
View Journal

Cite this: DOI: 10.1039/d5nj03842a

A diesel soot-derived high-performance anode material for lithium/sodium-ion batteries: impact of different annealing temperatures

Heng-rui Liu, [a] Qing-yang Bai[a] and Chao Ma *[b]

Received 26th September 2025,
Accepted 10th March 2026

DOI: 10.1039/d5nj03842a

rsc.li/njc

The development of high-performance anode materials is crucial for advancing next-generation electrochemical energy storage devices. Amorphous carbon materials (ACMs) have attracted significant attention as anodes for lithium-ion batteries (LIBs) and sodium-ion batteries (SIBs) due to their high reversible capacity and excellent stability. This study explores the use of diesel soot – typically toxic waste – as a precursor for ACMs. By varying the annealing temperature, we demonstrate that temperature plays a critical role in determining the material's properties and electrochemical performance. The soot treated at 900 °C (S-900) exhibits a high specific surface area (134.0 m^2 g^{-1}), a hierarchical porous structure, and excellent electrical conductivity. As an anode for LIBs, S-900 delivers an impressive reversible specific capacity of 626 mAh g^{-1} at 0.1 A g^{-1}, which increases to 640 mAh g^{-1} after 800 stable cycles at 1 A g^{-1}. In SIBs, S-900 shows a first-cycle reversible capacity of 241 mAh g^{-1} at 0.1 A g^{-1}, with 138 mAh g^{-1} retained after 1800 cycles at 1 A g^{-1}. This study provides a novel approach to the sustainable utilization of diesel soot.

Introduction

With the rapid growth of the global economy, the increasing reliance on fossil fuels has led to severe environmental concerns. Among the various pollutants produced by fuel combustion, particulate matter (PM) has been identified as a major health hazard, contributing to millions of deaths annually.[1] Diesel engine emissions, in particular, are a significant source of PM and have been classified as Group I carcinogens by the International Agency for Research on Cancer (IARC) since 2013.[2] According to the China Mobile Source Environmental Management Annual Report published by the Ministry of Ecology and Environment of the People's Republic of China, for the three consecutive years from 2021 to 2023, annual PM particulate emissions from motor vehicles nationwide reached 69 000, 59 000 and 44 000 t, respectively, with diesel vehicles accounting for more than 99% of the total PM emissions from automobiles each year. Currently, diesel particulate filters (DPFs) and electrostatic precipitators (ESPs) are the two primary technologies for controlling diesel exhaust particles (DEPs).[3,4] DPFs are popular due to their low cost and simplicity, but the cost of filter cleaning and regeneration, the risk of corrosion and fire due to carbon soot build-up, and the additional backpressure on the engine are yet to be resolved. ESPs, although effective, are unsuitable for smaller-scale applications due to their bulky equipment and maintenance demands. Soot, the major component of DEPs, is an unavoidable by-product of diesel combustion.[5] However, conventional treatment and disposal methods pose environmental hazards and fail to harness their potential value. Therefore, exploring sustainable and value-added strategies for soot recycling has become increasingly important.

Simultaneously, the global transition to renewable energy sources is accelerating, driven by the finite nature of fossil fuels. While solar and wind energy offer cleaner alternatives, their intermittent nature necessitates efficient energy storage technologies. LIBs currently dominate the market due to their high energy density, long lifespan, and environmental advantages. Nevertheless, challenges remain, including concerns over lithium resource availability, production cost, and operational safety. SIBs have emerged as a promising alternative owing to the abundance and low cost of sodium resources. As the anode plays a critical role in determining battery performance, the development of advanced anode materials is essential for both LIBs and SIBs. While conventional anodes such as silicon-, alloy-, and phosphide-based materials have been studied extensively, carbon-based anodes have gained attention due to their reversible capacity, structural stability, high conductivity, and tuneable porosity.[6–8] Graphite, the most established anode material for LIBs, is limited

[a] School of Mechanical Engineering, Shanghai Jiao Tong University, Shanghai, 200240, P. R. China
[b] College of Smart Energy, Shanghai Jiao Tong University, Shanghai, 200240, P. R. China. E-mail: chaoma99@sjtu.edu.cn

by its low theoretical capacity (372 mAh g^{-1}),[9] potential safety risks from lithium dendrite growth,[10] and poor compatibility with larger sodium ions which makes it unsuitable for sodium-ion systems.[11] To overcome these limitations, amorphous carbon materials (ACMs) have been explored as alternative anodes. For LIBs, porous ACMs were once used as the anode material and achieved a reversible capacity of 400 mAh g^{-1}, attributing the performance to the high surface area, rich porosity, and large interlayer spacing, which facilitated lithium storage and reaction kinetics.[12] For SIBs, hard carbon (a typical ACM) has shown promising cycling stability and sodium storage capacity (~300 mAh g^{-1}), making it a preferred choice.[13] A variety of carbon-rich precursors, such as biomass,[14,15] coal[16,17] and petroleum derivatives,[18,19] have been investigated for synthesizing ACM-based anodes. Soot, composed of more than 80% carbon[20] and typically forming amorphous nanospheres, has also been recognized as a viable precursor. The potential of candle soot was demonstrated as a LIB anode to achieve a stable capacity of 170 mAh g^{-1} after 1000 cycles at 10C.[21] After being further improved by annealing, the candle soot materials achieved reversible specific capacities as high as 1247 mAh g^{-1} for LIBs and 461 mAh g^{-1} for SIBs.[22] Despite these advances, candle soot differs significantly from diesel soot in origin and the production method, limiting its relevance for large-scale applications. More practically, diesel soot from in-service engines has shown potential. Soot deposits from low-quality heavy fuel oil-fuelled diesel engines on merchant ships were treated and achieved 260 mAh g^{-1} after 150 cycles by graphitizing at 2700 °C.[23] Similarly, soot particles derived from the combustion of light diesel oil (LDO) on warships, treated at 1000 °C, delivered capacities of 544 and 485 mAh g^{-1} at 0.1 and 1C, respectively.[24] These findings demonstrate the high carbonization degree of diesel soot and its potential for efficient conversion into anode materials. However, critical questions remain regarding whether diesel soot from smaller-scale engines can be feasibly recycled, how does annealing temperature affect the structure and performance of the resulting carbon materials, and whether diesel soot can be effectively applied in SIBs.

In this study, we focus on these questions by systematically investigating the effect of annealing temperature on the properties and performance of diesel soot-derived anodes. Soot was collected from a light diesel oil powered excavator engine and annealed at 800, 900 and 1000 °C. The resulting materials were characterized for their physical, chemical, and electrochemical properties to identify the optimal treatment condition (Fig. 1). This work highlights the potential of diesel soot as a sustainable and high-performance anode material for both LIBs and SIBs. By establishing the critical role of annealing temperature, we provide fundamental insights for optimizing soot recycling processes and advancing the development of environmentally responsible energy storage technologies.

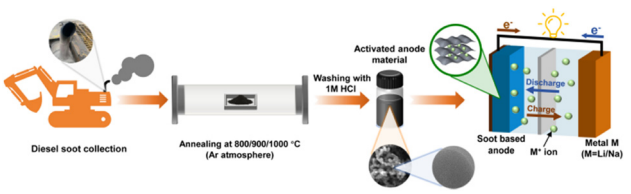

Fig. 1 Schematic illustration of collection, activation and application of soot materials for batteries.

Experimental

Diesel soot collection

Diesel soot was collected using a standardized protocol to ensure batch-to-batch reproducibility. Soot samples were mechanically scraped from the inner surface of the exhaust outlet of diesel engines (Huadong Engine Co., China) compliant with the China IV Emission Standard. The engines operated on light diesel oil (LDO) under consistent pre-collection conditions. To minimize variability, all collections were performed at the same location within the exhaust system using identical procedures. The soot was sourced from diesel engines with identical specifications, including the same engine model, the fuel type (standard no. 0 diesel), comparable factory ages, and similar operational profiles. The raw soot (S-raw), appearing as black powdery deposits, was used directly as the precursor material. Detailed engine specifications are provided in Table S1.

Activated carbon preparation

The collected soot was first dried and then subjected to thermal treatment in a tubular furnace under a 99% argon atmosphere. The furnace temperature was raised at a rate of 5 °C min^{-1} to 800, 900, or 1000 °C, held at target temperature for 2 hours, and then allowed to cool naturally to room temperature. After annealing, the soot was washed with a 1 M HCl solution at a ratio of 1 g of soot powder to 50 mL of HCl. The mixture was stirred at room temperature (25 °C) for 4 h. Subsequently, the sample was rinsed with deionized water 3–4 times until neutral pH was reached, followed by suction filtration. The filter residue was then dried at 80 °C for 48 h to obtain the acid-washed soot sample. The final carbon materials were labelled S-800, S-900, and S-1000 based on the respective annealing temperature.

Material characterization

The crystal structure of the soot-derived carbon materials was analysed using X-ray diffraction (XRD, Rigaku MiniFlex) with Cu Kα radiation (λ = 1.5406 Å) operated at 45 kV and 30 mA. Data were collected over a 2θ range of 15–80° at a scan rate of 10° min^{-1}. Raman spectroscopy (Renishaw Raman Spectroscope, inVia Qontor) was performed using a 532 nm laser to examine structural disorder and defects. Each spectrum was collected with an integration time of 10 seconds and averaged over three accumulations. The surface area and porosity were assessed using nitrogen adsorption–desorption isotherms measured at 77 K with a Micromeritics ASAP 2460 analyser (3Flex Version 5.03, Micromeritics). Prior to testing, the samples were degassed at 200 °C under a N_2 atmosphere for 6 hours. Pore size distributions were calculated using the Barrett–Joyner–Halenda (BJH) method. Morphological analysis was conducted using a

scanning electron microscope (SEM, ZEIS EVO 10) at an acceleration voltage of 5 kV. High-resolution transmission electron microscopy (HRTEM, JEOL JEM-2100F) was performed at 200 kV to further examine the microstructure of the carbon materials. The elemental composition was determined using inductively coupled plasma optical emission spectrometry (ICP-OES, Avio 500) to quantify the efficiency of impurity removal.

Electrode fabrication and characterization

To prepare the electrodes, the activated carbon was mixed with Super P conductive carbon and a polyvinylidene fluoride (PVDF) binder in a mass ratio of 8 : 1 : 1. The mixture was ground using an agate mortar, dried at 80 °C, and then dispersed in *N*-methyl-2-pyrrolidone (NMP) to form a uniform slurry. The slurry was cast onto polished copper foil using a doctor blade with a 100 μm gap and dried under vacuum at 80 °C overnight. The resulting electrodes had a mass loading of approximately 1.0–1.2 mg cm^{-2}. For lithium-ion battery (LIB) testing, CR2016 coin cells were assembled in an argon-filled glovebox (O_2 < 0.01 ppm and H_2O < 0.1 ppm), with the carbon-coated electrode as the working electrode, the lithium metal as the counter electrode, and a polypropylene (PP) separator (Celgard 2400). The electrolyte used was 1 M $LiPF_6$ dissolved in a 1 : 1 volume ratio of ethylene carbonate (EC) and dimethyl carbonate (DMC). For sodium-ion battery (SIB) testing, the slurry preparation followed the same procedure, except that sodium alginate was used as the binder while maintaining the 8 : 1 : 1 mass ratio. CR2016 coin cells were similarly assembled, using the sodium metal as the counter electrode, a 1 M $NaClO_4$ solution in ethylene carbonate (EC)/diethyl carbonate (DEC) (1 : 1 v/v) as the electrolyte, and a glass fibre separator.

Electrochemical performance was evaluated using cyclic voltammetry (CV) and electrochemical impedance spectroscopy (EIS), carried out on a Chenhua workstation (CHI660e). Galvanostatic charge/discharge cycling tests were performed using a Neware BTS4000 battery test system. CV and charge/discharge tests were conducted in the voltage window of 0.01–3.0 V (*vs.* Li^+/Li or Na^+/Na) at room temperature (25 °C). The current rate was normalized to the mass of active material (A g^{-1}). EIS measurements were recorded with a 10 mV AC amplitude over a frequency range of 100 kHz to 0.1 Hz.

Results and discussion

To investigate the crystal structure of the annealed soot materials, X-ray diffraction (XRD) and Raman spectroscopy were performed. As shown in Fig. 2a, the XRD patterns of all the samples exhibit two broad peaks centred around 2θ = 26° and 43°, corresponding to the (002) and (100) planes of graphite, respectively. The (002) plane represents parallel stacking of graphene layers, while the (100) plane reflects the in-plane honeycomb lattice of sp^2-hybridized carbon atoms.[25] The broad nature of these peaks suggests that the soot-derived materials are predominantly amorphous carbon containing localized graphitic domains with limited ordering, typically extending only a few nanometres.[26] With increasing annealing temperature, the (002) peak shifts slightly toward higher angles, indicating a reduction in interlayer spacing. Based on Bragg's equation ($2d \sin\theta = n\lambda$), the calculated interlayer distances (d_{002}) for S-800, S-900, and S-1000 are 3.55, 3.52 and 3.50 Å, respectively. This trend implies enhanced graphitization at the higher annealing temperature. Notably, these values remain

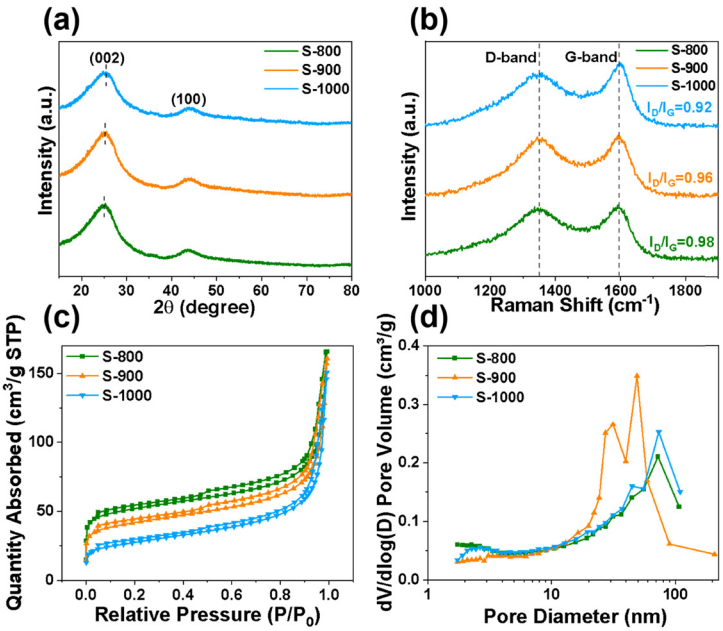

Fig. 2 (a) XRD patterns, (b) Raman spectra, (c) nitrogen adsorption and desorption isotherms and (d) BJH pore size distribution of S-800, S-900 and S-1000.

larger than the typical interlayer spacing of graphite (3.35 Å),[27] which may promote more efficient lithium/sodium ion insertion and extraction, contributing to improved reversible capacity and ion transport kinetics. Raman spectra of the samples are presented in Fig. 2b. All spectra exhibit two characteristic bands: the D band ($\sim$1340 cm^{-1}), associated with disordered or defective sp^2 carbon structures, and the G band ($\sim$1580 cm^{-1}), which arises from the in-plane vibrational mode of graphitic carbon.[28] The ratio (I_D/I_G) serves as an indicator of structural disorder and graphitization. For S-800, S-900, and S-1000, the I_D/I_G values are 0.98, 0.96, and 0.92, respectively. A decreasing trend in this ratio with increasing temperature confirms progressive conversion of amorphous carbon to a more ordered graphitic structure. Nevertheless, the relatively high I_D/I_G values, compared to those of highly crystalline graphite, indicate that the materials retain a significant degree of disorder, typical of ACMs. These structural defects are beneficial for electrochemical performance, offering additional active sites for ion storage and enhancing reversible capacity.

The nitrogen adsorption–desorption isotherms and pore size distribution of the annealed soot samples are shown in Fig. 2c. All samples display type IV nitrogen adsorption–desorption isotherms. In the low-pressure region (P/P_0 = 0.01–0.1), a sharp increase in adsorption volume is observed, particularly for S-800 and S-900, indicating the presence of micropores (pore diameter <2 nm). In the mid-pressure range (P/P_0 = 0.1–0.9), the isotherms display H3-type hysteresis loops, marked by steep and parallel adsorption and desorption branches. This feature is typically associated with disordered slit-like pores formed by the stacking of lamellar carbon structures—commonly seen in amorphous graphite-like materials. At high relative pressures (P/P_0 = 0.9–0.99), the absence of a distinct adsorption plateau suggests a broad and uneven pore size distribution, further confirming a hierarchical porous architecture.

The Brunauer–Emmett–Teller (BET) surface areas for S-800, S-900, and S-1000 are 163.6, 134.0 and 91.4 $m^2\ g^{-1}$, respectively, showing a clear decrease with increasing annealing temperature. This reduction is attributed to the collapse or coalescence of pores at higher temperatures. As the annealing temperature increases, fragile pore structures tend to shrink or collapse under thermal stress, while neighboring pores may coalesce into larger ones through atomic rearrangement. Both processes are thermally driven and result in a reduced total pore surface area, thereby lowering the BET surface area values. The pore size distribution (Fig. 2d), calculated using the Barrett–Joyner–Halenda (BJH) method, reveals a broad hierarchical structure spanning the mesopore (pore diameter = 2–50 nm) to macropore (pore diameter >50 nm) ranges. S-900 exhibits the highest mesopore content, while S-800 and S-1000 show slightly more pronounced macropore presence. The hierarchical porous architecture facilitates ion transport and electrolyte penetration, which are key to achieving high-rate electrochemical performance. Compared to conventional graphite, which typically exhibits BET surface areas below 2 $m^2\ g^{-1}$, the much higher specific surface areas of soot-derived carbon enhance electrode–electrolyte interactions. This improvement supports fast ion transport and contributes to high conductivity and rate capability.[29] Further pore structure analysis using non-local density functional theory (NLDFT), shown in Fig. S1, confirms the existence of micropores, along with internal cavities and defects. Consistent with the BET results, the micropore volume data in Table S2 show a clear downward trend with increasing temperature. The average pore diameter of S-1000 (15.1 nm) is notably larger than that of S-800 (12.9 nm) and S-900 (13.7 nm), while the micropore volume of S-800 (0.048 $cm^3\ g^{-1}$) and S-900 (0.033 $cm^3\ g^{-1}$) is significantly greater than that of S-1000 (0.014 $cm^3\ g^{-1}$). These results reflect the partial collapse and merging of pores at elevated temperature and further indicate that the S-1000's pore structure is primarily composed of macropores. Since the micropore network significantly influences the surface area, the reduction of micropore volume directly impacts the material's textural properties. Moreover, the presence of hierarchical pores in the meso- and macropore range allows for rapid electrolyte access and ion diffusion, while micropores in the 0.5–1.5 nm range have been shown to accommodate lithium deposition. The abundance of such microstructures in the soot-derived materials can therefore provide ample active sites, leading to enhanced reversible capacity.[30]

In addition, to elucidate the structural enhancement induced by the preliminary annealing treatment, the specific surface area and pore structure of S-raw were systematically characterized. According to the BET analysis, S-raw exhibits a low specific surface area of 49.86 $m^2\ g^{-1}$, a total pore volume of 0.161 $cm^3\ g^{-1}$, an average pore diameter of 15.89 nm, and an extremely limited micropore volume of only 0.0081 $cm^3\ g^{-1}$. Compared with the samples annealed at elevated temperatures (S-800, S-900 and S-1000), both the specific surface area and micropore volume of S-raw are significantly lower, indicating a poorly developed pore structure, particularly with respect to micropores. As shown in the nitrogen adsorption–desorption isotherm of S-raw (Fig. S2a), the isotherm can be classified as Type II, suggesting that the material is predominantly nonporous or macroporous, with only minor contributions from mesopores and micropores. The corresponding BJH pore size distribution (Fig. S2b) further confirms that the pore population of S-raw is mainly concentrated in the macropore region, with a notable deficiency of *g* effective mesoporous and microporous structures. In addition, the micropore size distribution plot (Fig. S2c) indicates a negligible micropore volume, further corroborating the underdeveloped pore architecture of the raw carbon soot material. In contrast, after high-temperature annealing treatment, the specific surface area, total pore volume, and micropore volume of the samples increase substantially, accompanied by a decrease in average pore diameter. The results demonstrate that the annealing process effectively promotes pore formation and structural evolution, particularly by significantly enhancing the development of micropores and mesopores.

The morphology and microstructure of the soot-derived carbon materials were characterized by scanning electron microscopy (SEM) and high-resolution transmission electron microscopy (HRTEM). SEM images of S-800, S-900, and S-1000,

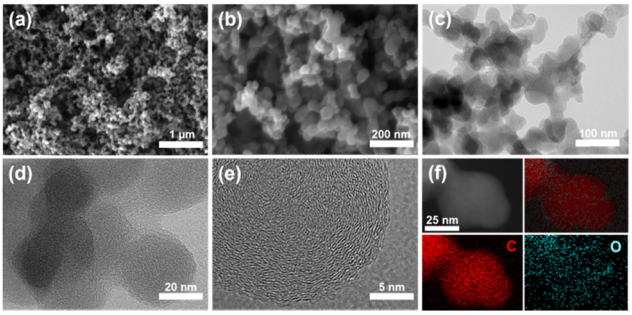

Fig. 3 (a) and (b) SEM images, (c)–(e) HRTEM images and (f) EDS mapping images of S-900.

shown in Fig. 3a and b and Fig. S3, reveal that all samples consist of densely packed, homogeneous nanospheres with diameters ranging from 45 to 65 nm. No significant differences in particle size, shape, or stacking behaviour are observed across the different annealing temperatures. Further insight into the internal structure was obtained from HRTEM analysis of the S-900 sample, shown in Fig. 3c and d. The images show that the spherical nanoparticles are interconnected through diffusion bonding and/or adhesion, forming interwoven chains and mesh-like structures. This interconnected network is expected to facilitate efficient electron and ion transport by reducing diffusion pathways, thereby enhancing the electrical conductivity of the material.[31] The HRTEM images also reveal characteristic turbostratic features – disordered, fingerprint-like graphite layers with short-range ordering – typical of amorphous carbon materials (ACMs). These turbostratic structures not only enable lithiation at relatively high potentials but also offer numerous disordered interlayer gaps, which provide additional active sites for lithium ion storage.[32] Elemental composition analysis using energy-dispersive X-ray spectrometry (EDS), shown in Fig. 3f, confirms that the soot material primarily consists of carbon (96.16 wt%) with a minor amount of uniformly distributed oxygen (3.84 wt%). The presence of oxygen-containing functional groups may further enhance the electrochemical reactivity and wettability of the material.

ICP-OES analysis was performed to quantify the concentrations of selected impurity elements (Fe, Ca, Zn, S, and Si) in the soot materials in order to evaluate the effectiveness of the acid washing step. These elements were selected based on previous reports identifying them as representative impurities in diesel engine soot which may affect electrochemical performance.[33,34] The analysis covered S-raw, pre-washed samples (Pr-S-800, Pr-S-900 and Pr-S-1000) and acid-washed samples (S-800, S-900 and S-1000), as summarized in Table S3. For Fe and Ca, the removal efficiency exceeded 90% after acid washing; for example, in S-900, the Fe content decreased from 1.415 wt% (Pr-S-900) to 0.069 wt%, and the Ca content from 1.044 wt% to 0.077 wt%. The concentrations of other elements (Zn, S, and Si) were below 0.05 wt% in all washed samples, indicating a negligible influence on material performance. These results confirm that the acid washing process effectively removes critical impurities, thereby enhancing the reliability of the electrochemical results.

To assess the electrochemical performance of the soot-derived carbon materials, galvanostatic charge/discharge tests were conducted on half-cells over a voltage window of 0.01 to 3.0 V. As shown in Fig. 4a and Fig. S4a and b, the initial reversible capacities for S-800, S-900 and S-1000 were 465, 626, and 524 mAh g^{-1}, with initial coulombic efficiencies (ICE) of 61%, 63%, and 59%, respectively. The charge/discharge curves exhibit sloping profiles without obvious plateaus, which differs from the typical behaviour of graphite anodes. This feature, combined with capacities exceeding the theoretical limit of graphite (372 mAh g^{-1}), indicates a strong capacitive contribution, characteristic of porous amorphous carbon. The relatively low ICEs can be attributed to the two factors: (i) the porous structure of the soot-derived materials allows lithium ions to be trapped during the first discharge, preventing full reversibility, and (ii) the high specific surface area facilitates extensive solid electrolyte interphase (SEI) formation, consuming lithium during initial cycles. However, the trapped lithium can contribute to SEI repair in later cycles, gradually stabilizing performance. Cyclic voltammetry (CV) tests of S-900 at a scan rate of 0.1 mV s^{-1} (Fig. 4b) show a broad irreversible reduction peak between 0.6 and 1.6 V in the first cycle, corresponding to SEI formation, lithium insertion into disordered carbon domains, and partial electrolyte decomposition.[35] This is consistent with the high initial discharge capacity and low ICE. In subsequent cycles, the reduction peak disappears and the CV curves overlap closely, indicating stable and reversible electrochemical behaviour. A sharp reduction peak at ~0.01–0.5 V reflects lithium interpolation into graphite-like domains, while the corresponding oxidation peak at ~0.25 V represents lithium extraction. Additional peaks at ~0.5 V (reduction) and ~1.1 V (oxidation) are attributed to surface adsorption/desorption processes. The relatively higher lithiation potential suggests enhanced safety compared to commercial graphite, as it reduces the risk of lithium dendrite formation. Fig. 4c presents the cycling performance at 0.1 A g^{-1}. All three materials quickly stabilize after five cycles, with coulombic efficiencies exceeding 95% and approaching 100% after 20 cycles. At the 100th cycle, the S-800, S-900, and S-1000 retained reversible capacities of 372, 499, and 493 mAh g^{-1}, respectively, with capacity retention rates of approximately 80%, 80%, and 94%. The rate capabilities of the materials were tested at varying current densities from 0.05 to 2 A g^{-1}, as shown in Fig. 4d and Table S4. S-900 consistently outperformed S-800 and S-1000 at each C-rate. The capacity retention at 1 A g^{-1}, relative to 0.1 A g^{-1}, was 68% for both S-800 and S-900 and 76% for S-1000. Upon returning to 0.1 A g^{-1} after high-rate cycling, all samples recovered their original capacity, indicating good reversibility and structural stability. To further elucidate the rate capability, the galvanostatic charge–discharge profiles of S-800, S-900, and S-1000 at current densities ranging from 0.05 to 2 A g^{-1} were analyzed, as shown in Fig. S5. These curves correspond to the 3rd, 8th, 13th, 18th, 23rd, and 28th cycles of the rate performance test presented in Fig. 4(d). The profiles of S-800 exhibit increasing voltage polarization and a more sloping voltage plateau at high current densities, indicating pronounced kinetic limitations. In contrast, S-900 demonstrates reduced polarization and better

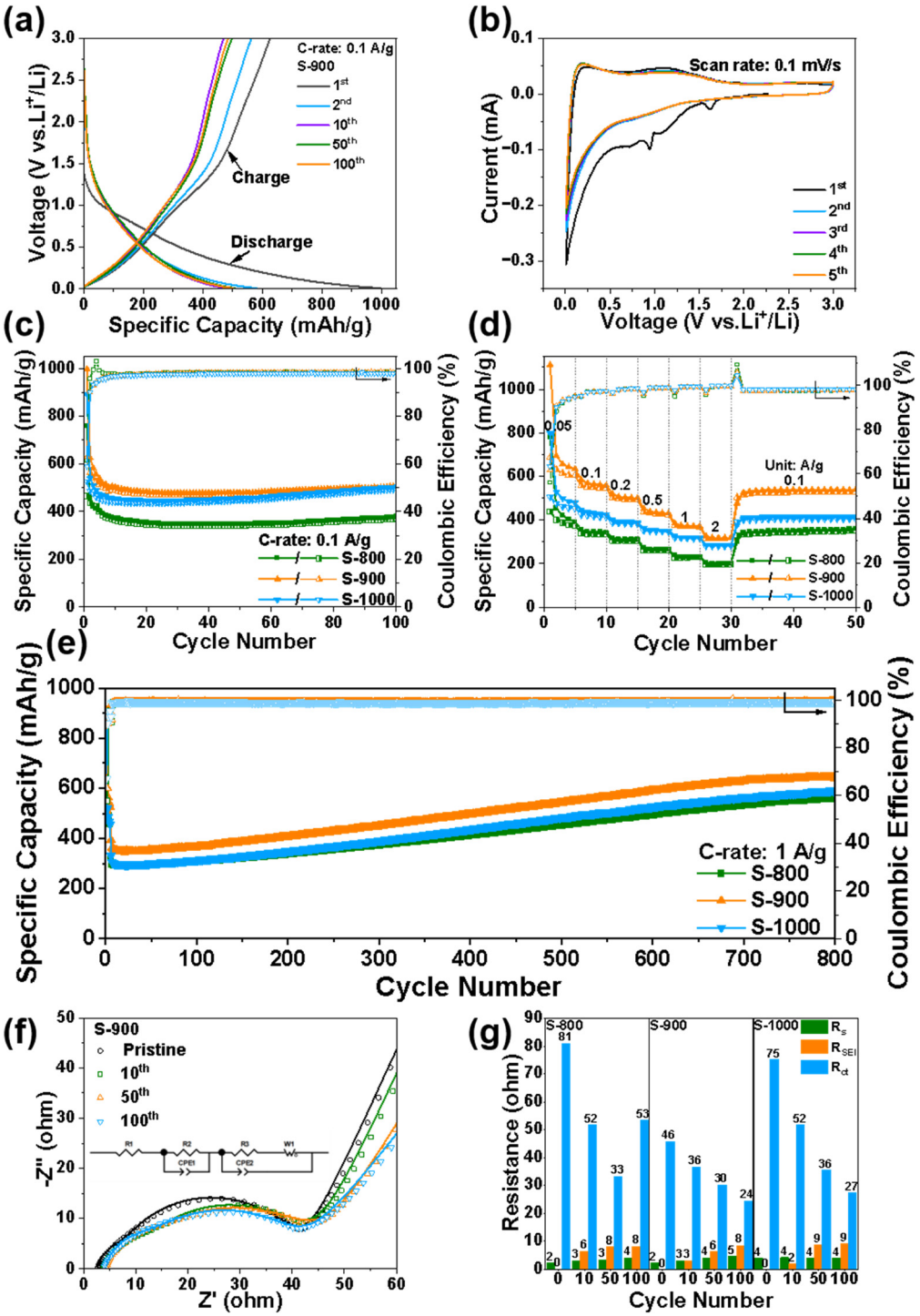

Fig. 4 (a) Charge/discharge profiles of S-900 and (b) cyclic voltammograms of the initial five cycles at a scan rate of 0.1 mV s^{-1}. (c) Cyclic performance at a current density of 0.1 A g^{-1}, (d) rate performance and (e) long cyclic performance. (f) Nyquist plots of S-900. (g) Histogram of the R_s, R_{SEI}, and R_{ct} of S-800, S-900 and S-1000.

capacity retention, suggesting improved ion transport associated with the optimized annealing temperature. Notably, S-1000 maintains well-defined plateaus and the lowest polarization even at 2 A g^{-1}, highlighting its superior kinetics derived from enhanced graphitization and electrical conductivity. This progressive improvement in electrochemical kinetics is fully consistent with the rate performance results shown in Fig. 4(d). Long-term cycling performance was further evaluated at 1 A g^{-1} after an initial activation phase of five cycles at 0.1 A g^{-1}. As shown in Fig. 4e, all three samples displayed a gradual increase in specific capacity during the first 700 cycles, stabilizing thereafter. At the 6th cycle (first cycle at 1 A g^{-1}), S-800, S-900, and S-1000 delivered reversible

capacities of 295, 363, and 300 mAh g^{-1}, which increased to 556, 640, and 586 mAh g^{-1}, respectively, by the 800th cycle – nearly doubling their initial values. This capacity increase is attributed to a continuous activation process, during which trapped lithium becomes electrochemically active and contributes to reversible capacity. Additionally, the SEI layer stabilizes progressively, enhancing long-term performance. This phenomenon is commonly observed in amorphous carbon materials with hierarchical porosity.[24] Throughout the 800-cycle test, coulombic efficiencies remained above 99%, confirming the high cycling stability of the materials under high current conditions. Electrochemical impedance spectroscopy (EIS) was performed on all three half-cells at various stages of cycling (Fig. 4f and Fig. S6a and b). Nyquist plots display semicircles in the high-frequency region (representing interfacial resistance) and straight lines in the low-frequency region (reflecting ion diffusion). The equivalent circuit model (inset of Fig. 4f) includes the following: (i) solution resistance (R_s, corresponding to R_1 in the circuit diagram), (ii) SEI resistance (R_{SEI}, corresponding to R_2), (iii) charge transfer resistance (R_{ct}), (iv) constant phase elements (CPE, corresponding to CPE_1 and CPE_2), and (v) Warburg impedance (Z_w, corresponding to W_1) associated with lithium-ion diffusion. As cycling progresses, the semicircular diameter in the Nyquist plots decreases, indicating reduced R_{ct} and gradual electrode activation. Meanwhile, R_{SEI} increases slowly due to stable SEI development. These trends, consistent with the capacity growth observed during long-term cycling, highlight the materials' excellent interfacial conductivity and lithium-ion diffusion properties. Among the three samples, S-900 consistently exhibited the lowest R_{ct}, further supporting its superior electrochemical performance (Fig. 4g and Table S5).

All three soot-derived carbon materials demonstrate promising yet differentiated electrochemical performance in lithium-ion batteries, primarily governed by their distinct pore structures and graphitization resulting from different annealing temperatures. The superior and most balanced performance of S-900 originates from its optimized hierarchical porous architecture achieved at 900 °C, in which micropores, mesopores, and macropores operate synergistically. Specifically, abundant micropores provide a high specific surface area and numerous active sites for lithium-ion adsorption and additional capacitive storage, which is crucial for achieving high capacity. The well-developed mesopores act as efficient ion transport pathways, enabling rapid lithium-ion diffusion to the interior active sites and thereby ensuring excellent rate capability. Meanwhile, macropores serve as electrolyte reservoirs, facilitating electrolyte infiltration and reducing ion diffusion distances. This hierarchical pore system, together with a moderate degree of graphitization that enhances electrical conductivity, collectively ensures efficient ion storage, fast reaction kinetics, and robust cycling stability. In contrast, S-800 suffers from incomplete graphitization and poorly connected pores, resulting in higher impedance. Although S-1000 shows enhanced graphitization, the severe collapse of micropores reduces the number of active sites for lithium storage, while the more compact graphite structure hinders ion intercalation. Therefore, the outstanding performance of S-900 can be attributed to the optimal balance achieved at 900 °C, which simultaneously optimizes ion-accessible porosity for kinetic advantages and a conductive framework for electronic percolation.

Furthermore, a systematic analysis of the rate performance of S-raw, the pre-washed samples and annealed samples (Fig. S7 and Table S4) is conducted to more exhaustively evaluate the effects of annealing and acid washing treatments on enhancing the electrochemical performance of diesel soot-derived carbon materials.

The S-raw sample exhibited severely limited performance, delivering only 224 mAh g^{-1} at 0.1 A g^{-1} and dropping sharply to 28 mAh g^{-1} at 2 A g^{-1}, accompanied by rapid capacity decay during the initial cycles and extremely low coulombic efficiency. This behaviour indicates pronounced irreversible interfacial reactions and sluggish ion/electron transport, originating from both an underdeveloped pore structure and the presence of impurity species. After annealing, the electrochemical performance of Pr-S-800, Pr-S-900, and Pr-S-1000 was markedly improved. For instance, Pr-S-900 delivered 537 mAh g^{-1} at 0.1 A g^{-1} and maintained 194 mAh g^{-1} at 2 A g^{-1}. This enhancement is mainly attributed to the optimized pore structure generated during annealing, including increased micropore and mesopore fractions, which provide more active sites and shortened ion-transport pathways. Importantly, compared with annealing alone, the subsequent acid-washing step led to a further improvement in interfacial kinetics, especially at high current densities. While the capacity difference between pre-washed and acid-washed samples is relatively small at low rates, it becomes much more pronounced at high rates. For example, after impurity removal, S-900 delivers 318 mAh g^{-1} at 2 A g^{-1}, which is substantially higher than that of Pr-S-900 (194 mAh g^{-1}) under the same conditions. This trend can be directly correlated with the ICP-OES results. Residual impurities such as Fe and Ca can act as catalytic centres for electrolyte decomposition, triggering irreversible side reactions, accelerating SEI growth, and producing a thicker, inhomogeneous SEI layer, thereby increasing interfacial resistance (R_{ct}) and causing capacity loss – effects that are particularly detrimental at high rates where ion transport is already kinetically limited. After acid washing, the significant reduction in impurity content suppresses these side reactions, promotes the formation of a thinner and more stable SEI, improves interfacial charge-transfer kinetics, and enhances ion diffusion efficiency, leading to improved rate capability and capacity retention. In addition, acid washing removes inorganic residues from the carbon surface, exposing cleaner carbon surfaces and accessible pore structures. This not only reduces active-site blockage but also increases the number of effective adsorption/storage sites, further contributing to the improved high-rate performance.

Moreover, to highlight the advantages of our diesel soot-derived carbon material, we compared its performance with that of previously reported carbon-based anodes (Table S6). In terms of the carbon source, our material is derived from diesel soot, representing the upcycling of hazardous waste with significant environmental benefits. In contrast, many reported materials rely on biomass precursors (*e.g.*, mangrove-charcoal

and rice straw) or specific waste sources (*e.g.*, human hair and candle soot), which may involve additional resource consumption or processing costs. Regarding electrochemical performance, the S-900 sample achieves a charge capacity that is higher than those of many biomass-derived carbons and soot-based carbons reported in the literature. This comparison demonstrates that our material achieves competitive or superior capacity while simultaneously enabling waste valorisation, thereby effectively balancing electrochemical performance and environmental sustainability.

To further explore the lithium storage mechanism of the soot-derived material and understand its excellent rate performance, the CV curve measurements were conducted at various scan rates of 0.1, 0.2, 0.4, 0.6, 0.8, and 1.0 mV s^{-1}, as shown in Fig. 5a. As the scan rate increased, the current response also increased. Even at the highest rate of 1.0 mV s^{-1}, distinct oxidation and reduction peaks remained visible, highlighting the materials' excellent rate capability.

To gain insight into the underlying kinetics, the relationship between peak current (i) and the scan rate (v) was analysed using the power law equation:[36–38]

$$i = av^b$$

$$\log i = b \log v + \log a$$

where a and b are constants. The slope b of the log(i) *vs.* log(v) plot, presented in Fig. 5b, indicates the dominant charge storage mechanism. For this material, the b values for the oxidation and reduction peaks are 0.77 and 0.94, respectively. A b value near 0.5 suggests diffusion-controlled behaviour, while an a value near 1.0 indicates a capacitive process. These results suggest a mixed charge storage mechanism with a strong capacitive contribution.

The relative contributions from diffusion-controlled and capacitive processes were further quantified using the following equation:[39–41]

$$i(V) = k_1 v + k_2 v^{1/2}$$

where $k_1 v$ represents the capacitive effect and $k_2 v^{1/2}$ the diffusive-controlled contribution. As shown in Fig. 5c and d, the capacitive contribution of the S-900 material increases with the scan rate, reaching 61%, 69%, 75%, 80%, 84%, and 87% at 0.1 to 1.0 mV s^{-1}, respectively. This trend confirms that capacitive processes dominate at higher rates, contributing significantly to the material's reversible capacity under rapid charge–discharge conditions. The strong capacitive behaviour is primarily attributed to the rapid adsorption of lithium ions onto the carbon surface, which occurs much faster than the diffusion-based intercalation into the graphite layers. Furthermore, the abundant surface adsorption sites offer additional reversible storage capacity. These findings underscore the electrochemical advantages conferred by the nanosphere architecture and high surface area of the soot-derived material, explaining its outstanding rate capability and high reversible capacity.

To further investigate the potential of soot-derived materials in alkali metal ion energy storage systems, we evaluated the electrochemical performance of sodium-ion half-cells assembled with the S-900 material (denoted as S-900-SIBs). Fig. S8 presents the charge–discharge profiles for the 1st, 2nd, 10th, 50th, and 100th cycles.

The S-900-SIBs deliver an initial reversible capacity of 241 mAh g^{-1}, and the nearly overlapping curves in subsequent

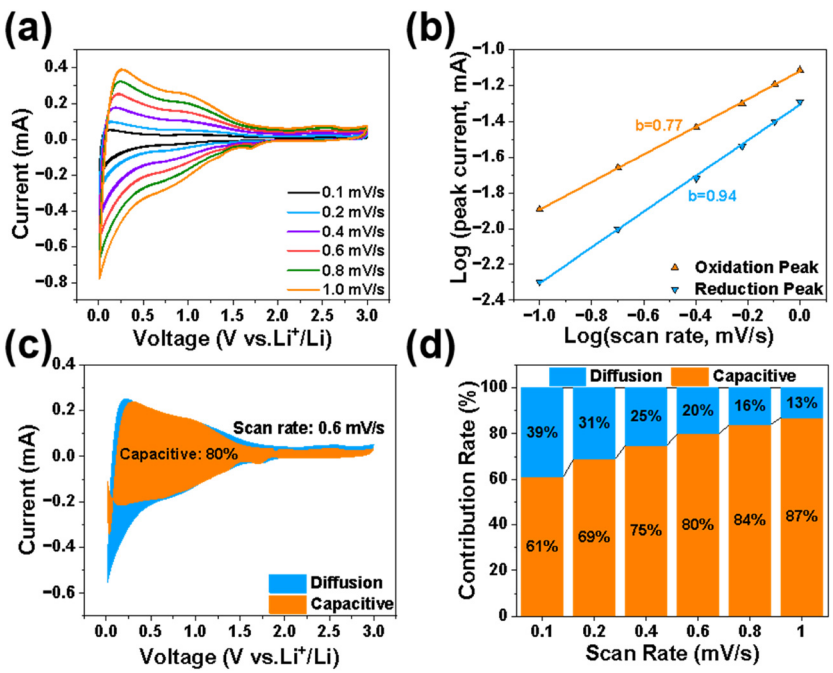

Fig. 5 (a) CV curves at various scan rates from 0.1 to 1.0 mV s^{-1}, (b) the fitting line and linear relationship of the anodic and cathodic log (peak current) and the log (scan rate) for calculating the b values, (c) CV curve with the capacitive contribution (orange shaded area) at 0.6 mV s^{-1} and (d) the ratio of capacitive contribution to the total capacity at various scan rates from 0.1 to 1.0 mV s^{-1} of S-900.

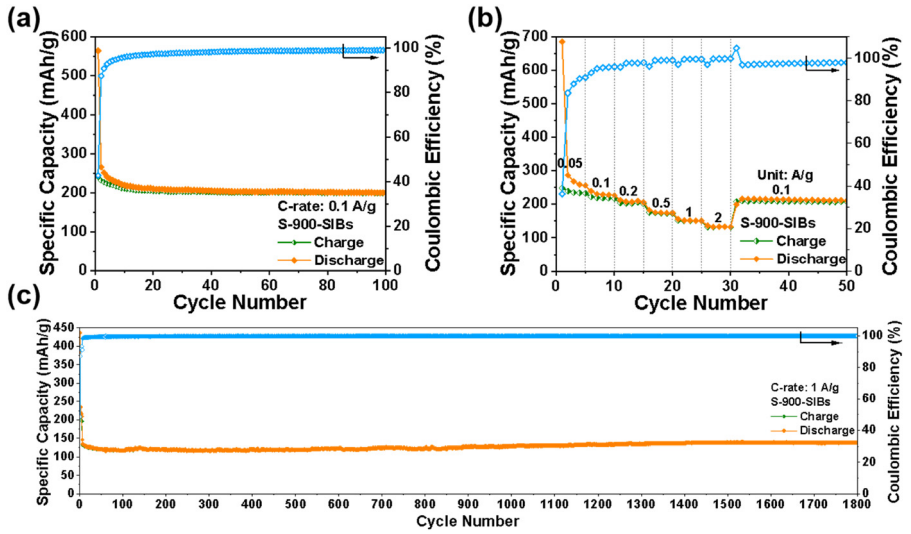

Fig. 6 The performance of S-900 within the SIB system: (a) cyclic performance at 0.1 A g^{-1}, (b) rate performance in the range of 0.05–2 A g^{-1}, and (c) cyclic performance at 1 A g^{-1}.

cycles indicate excellent reversibility and stability during sodium storage.

The presence of sloped regions in the voltage profiles suggests a predominant surface adsorption mechanism, facilitated by the material's porous structure and high specific surface area, which offer abundant active sites for sodium ion accommodation.[7] Fig. 6a shows the cycling performance at a constant current density of 0.1 A g^{-1}. The cell maintains a specific capacity of 200 mAh g^{-1} after 100 cycles, with a capacity retention of 83% and a coulombic efficiency of approximately 99%, demonstrating robust cycling stability. As shown in Fig. 6b, the rate capability of the S-900-SIBs was also impressive. Reversible capacities of 235, 219, 202, 175, 151, and 133 mAh g^{-1} were achieved at current densities of 0.05, 0.1, 0.2, 0.5, 1, and 2 A g^{-1}, respectively. Notably, the capacity at 1 A g^{-1} retained 69% of that at 0.1 A g^{-1}, and upon returning to 0.1 A g^{-1}, the capacity quickly recovered to its original level, indicating good structural integrity and electrochemical reversibility. Following five cycles of activation at 0.1 A g^{-1}, the long-term cycling performance was assessed at 1 A g^{-1}, as shown in Fig. 6c. The coulombic efficiency remained consistently above 99% from the 13th to the 1800th cycle, reaching 99.9% at the 1800th cycle. The reversible capacity remained stable, with a value of 138 mAh g^{-1} at the1800th cycle – closely matching the 132 mAh g^{-1} recorded at the 6th cycle. These results confirm that the S-900 material, with its expanded graphene interlayer spacing, porous hierarchical structure, and excellent electronic and ionic conductivity, offers high capacity, excellent rate performance, and long-term cycling stability in sodium-ion batteries. Therefore, diesel soot-derived carbon demonstrates significant potential as a high-performance anode material for sodium storage applications.

Conclusions

In conclusion, diesel soot – traditionally considered as a toxic waste – was successfully recycled and employed as a precursor to synthesize advanced amorphous carbon materials (ACMs) for use as high-performance anodes in LIBs and SIBs. A systematic investigation of the annealing temperature was conducted through a linear temperature gradient experiment to optimize the electrochemical performance of the resulting materials. Among the samples, the material annealed at 900 °C (denoted as S-900) exhibited the best overall performance. Compared with materials treated at higher temperature, S-900 possessed a larger specific surface area (134.05 m^2 g^{-1}), a rich microporous structure, and an expanded graphite interlayer spacing (d_{002} = 3.52 Å), which together provide ample active sites and ion diffusion channels for lithium storage. As a result, S-900 delivered a high reversible capacity of 626 mAh g^{-1} at 0.1 A g^{-1}. In contrast to materials annealed at lower temperatures, S-900 exhibited improved graphitization, contributing to both high-capacity retention and superior rate capability – achieving 640 mAh g^{-1} after 800 cycles at 1 A g^{-1}. S-900 as an anode for sodium-ion batteries showed a reversible capacity of 241 mAh g^{-1} at 0.1 A g^{-1}, along with excellent cycling stability, maintaining 138 mAh g^{-1} after 1800 cycles at 1 A g^{-1}. These results affirm the suitability of S-900 as a versatile and high-performance anode material for both LIBs and SIBs.

To broaden the impact and practical applicability of these findings, future research should evaluate the robustness of carbon materials derived from diverse soot sources (*e.g.*, from different fuels and combustion systems) to validate the universality of the annealing strategy and further enhance the scalability of soot-derived anodes for real-world energy storage applications.

Overall, this work not only elucidates the critical role of moderate annealing temperatures in regulating the structural evolution and electrochemical performance of soot-derived carbon materials but also establishes a sustainable and cost-effective strategy for upcycling hazardous waste into value-added functional materials. The insights gained from this study underscore the significance of this approach and provide

a robust foundation for guiding future research toward environmentally benign, high-performance battery technologies.

Author contributions

Liu Heng-rui conducted electrochemical tests and data analysis and wrote the initial manuscript; Liu Heng-rui and Bai Qingyang conducted diesel soot collection, activated carbon preparation and material characterization; Ma Chao proposed the project, supervised the work and revised the manuscript. All authors discussed the results and commented on the manuscript.

Conflicts of interest

The authors declare no conflicts of interest.

Data availability

The data that support the findings of this study are available from the corresponding author, Chao Ma, upon reasonable request. Supplementary information (SI): experimental data and the appendix. See DOI: https://doi.org/10.1039/d5nj03842a.

Acknowledgements

This work was financially supported by the Shanghai Municipal Science and Technology Major Project and the Startup Fund for Young Faculty at SJTU (22X010503814).

Notes and references

1 S. Shen, C. Li, A. van Donkelaar, N. Jacobs, C. Wang and R. V. Martin, *ACS ES&T Air*, 2024, **1**, 332–345.
2 Y. Yin, C. Mu, J. Wang, Y. Wang, W. Hu, W. Zhu, X. Yu, W. Hao, Y. Zheng, Q. Li and W. Han, *Toxics*, 2023, **11**, 646.
3 R. Walter, J. Neumann and O. Hinrichsen, *Environ. Sci. Technol.*, 2020, **54**, 9285–9294.
4 A. Sudrajad and A. F. Yusof, *Energy Procedia*, 2015, **68**, 370–380.
5 D. R. Tree and K. I. Svensson, *Prog. Energy Combust. Sci.*, 2007, **33**, 272–309.
6 N. A. Kaskhedikar and J. Maier, *Adv. Mater.*, 2009, **21**, 2664–2680.
7 X. Chen, C. Liu, Y. Fang, X. Ai, F. Zhong, H. Yang and Y. Cao, *Carbon Energy*, 2022, **4**, 1133–1150.
8 W. Ni and L. Shi, *J. Vac. Sci. Technol., A*, 2019, **37**, 040803.
9 J. Zhu, P. Li, X. Chen, D. Legut, Y. Fan, R. Zhang, Y. Lu, X. Cheng and Q. Zhang, *Energy Storage Mater.*, 2019, **16**, 426–433.
10 Q. Liu, C. Du, B. Shen, P. Zuo, X. Cheng, Y. Ma, G. Yin and Y. Gao, *RSC Adv.*, 2016, **6**, 88683–88700.
11 C. Fan, R. Zhang, X. Luo, Z. Hu, W. Zhou, W. Zhang, J. Liu and J. Liu, *Carbon*, 2023, **205**, 353–364.
12 G. Yang, X. Li, Z. Guan, Y. Tong, B. Xu, X. Wang, Z. Wang and L. Chen, *Nano Lett.*, 2020, **20**, 3836–3843.
13 S. Tan, H. Yang, Z. Zhang, X. Xu, Y. Xu, J. Zhou, X. Zhou, Z. Pan, X. Rao, Y. Gu, Z. Wang, Y. Wu, X. Liu and Y. Zhang, *Molecules*, 2023, **28**, 3134.
14 C. Hernández-Rentero, V. Marangon, M. Olivares-Marín, V. Gómez-Serrano, Á. Caballero, J. Morales and J. Hassoun, *J. Colloid Interface Sci.*, 2020, **573**, 396–408.
15 M. Ishaq, M. Jabeen, Y.-S. He, H. Che, W. Xu, S. Zhao, Y. Shen, L. Li and Z.-F. Ma, *Adv. Energy Mater.*, 2025, **15**, 2403142.
16 K. Wang, F. Sun, H. Wang, D. Wu, Y. Chao, J. Gao and G. Zhao, *Adv. Funct. Mater.*, 2022, **32**, 2203725.
17 S. Xu, J. Van Der Watt, D. Laudal, R. Zhang, R. Ahmed and X. Hou, *J. Power Sources*, 2025, **628**, 235858.
18 Y. Wang, W. Tian, L. Wang, H. Zhang, J. Liu, T. Peng, L. Pan, X. Wang and M. Wu, *ACS Appl. Mater. Interfaces*, 2018, **10**, 5577–5585.
19 J.-H. Lv, B. He, L.-T. Lv, M.-K. Yan, J.-C. Zhong, G.-P. Hao and W.-C. Li, *J. Power Sources*, 2025, **634**, 236505.
20 K. O. Johansson, M. P. Head-Gordon, P. E. Schrader, K. R. Wilson and H. A. Michelsen, *Science*, 2018, **361**, 997–1000.
21 M. Kakunuri and C. S. Sharma, *Electrochim. Acta*, 2015, **180**, 353–359.
22 R. Kanakaraj and C. Sudakar, *J. Power Sources*, 2020, **458**, 228064.
23 W.-J. Lee, H. V. Kim, J.-H. Choi, G. Panomsuwan, Y.-C. Lee, B.-S. Rho and J. Kang, *Sci. Rep.*, 2018, **8**, 5601.
24 H.-M. Baek, D.-Y. Kim, W.-J. Lee and J. Kang, *RSC Adv.*, 2020, **10**, 36478–36484.
25 C. Yang, J. Zhao, B. Dong, M. Lei, X. Zhang, W. Xie, M. Chen, K. Zhang and L. Zhou, *J. Mater. Chem. A*, 2024, **12**, 1340–1358.
26 B. Jache, C. Neumann, J. Becker, B. M. Smarsly and P. Adelhelm, *J. Mater. Chem.*, 2012, **22**, 10787.
27 C. Bommier, T. W. Surta, M. Dolgos and X. Ji, *Nano Lett.*, 2015, **15**, 5888–5892.
28 M. S. Dresselhaus, A. Jorio, M. Hofmann, G. Dresselhaus and R. Saito, *Nano Lett.*, 2010, **10**, 751–758.
29 J. He, N. Wang, Z. Cui, H. Du, L. Fu, C. Huang, Z. Yang, X. Shen, Y. Yi, Z. Tu and Y. Li, *Nat. Commun.*, 2017, **8**, 1172.
30 P.-Y. Chang and R. Doong, *J. Alloys Compd.*, 2019, **775**, 214–224.
31 S. Singh, P. K. Bairagi and N. Verma, *Electrochim. Acta*, 2018, **264**, 119–127.
32 V. Etacheri, C. Wang, M. J. O'Connell, C. K. Chan and V. G. Pol, *J. Mater. Chem. A*, 2015, **3**, 9861–9868.
33 A. Liati, D. Schreiber, P. Dimopoulos Eggenschwiler and Y. Arroyo Rojas Dasilva, *Environ. Sci. Technol.*, 2013, **47**, 14495–14501.
34 K. Saitoh, K. Sera, T. Shirai, T. Sato and M. Odaka, *Anal. Sci.*, 2003, **19**, 525–528.
35 H. Tabassum, R. Zou, A. Mahmood, Z. Liang, Q. Wang, H. Zhang, S. Gao, C. Qu, W. Guo and S. Guo, *Adv. Mater.*, 2018, **30**, 1705441.

36 I. Muhammad, M. Jabeen, P. Wang, Y.-S. He, X.-Z. Liao and Z.-F. Ma, *Dalton Trans.*, 2021, **50**, 4555–4566.
37 S. Alvin, H. S. Cahyadi, J. Hwang, W. Chang, S. K. Kwak and J. Kim, *Adv. Energy Mater.*, 2020, **10**, 2000283.
38 G. Zhao, D. Yu, H. Zhang, F. Sun, J. Li, L. Zhu, L. Sun, M. Yu, F. Besenbacher and Y. Sun, *Nano Energy*, 2020, **67**, 104219.
39 J. Wang, J. Polleux, J. Lim and B. Dunn, *J. Phys. Chem. C*, 2007, **111**, 14925–14931.
40 D. Chao, P. Liang, Z. Chen, L. Bai, H. Shen, X. Liu, X. Xia, Y. Zhao, S. V. Savilov, J. Lin and Z. X. Shen, *ACS Nano*, 2016, **10**, 10211–10219.
41 V. Augustyn, P. Simon and B. Dunn, *Energy Environ. Sci.*, 2014, **7**, 1597.